

# Faraday Acceleration with Radio-frequency Assisted Discharge (FARAD)

Edgar Y. Choueiri\* and Kurt A. Polzin†

Electric Propulsion and Plasma Dynamics Laboratory (EPPDyL)  
Mechanical and Aerospace Engineering Department  
Princeton University, Princeton, New Jersey 08544

AIAA-2004-3940‡

July 11-14, 2004

A new electrodeless accelerator concept that relies on an RF-assisted discharge, an applied magnetic field, and electromagnetic acceleration using an inductive coil is presented. The advantages of this concept include efficient plasma production, magnetic field guided mass injection, and electromagnetic acceleration by Lorentz forces that result from the interactions between the azimuthal current in an induced current sheet and *both* an induced and applied magnetic field. The concept is inherently more compact than the Pulsed Inductive Thruster and is promising for spacecraft propulsion. A proof-of-concept experiment has been constructed and used to demonstrate inductive coupling between the preionized plasma and a pulse of current flowing in a planar acceleration coil. Visual observations indicate that the plasma follows the applied magnetic field from the RF discharge to the face of the planar acceleration coil, magnetic field probing yields evidence of the motion of the current sheet and imaging using a fast-framing camera shows the formation and acceleration of the current sheet.

## I. INTRODUCTION

We first describe a new pulsed inductive accelerator concept, the **F**araday **A**ccelerator with **R**adio-frequency **A**ssisted **D**ischarge (FARAD), then list its advantages with respect to other concepts and provide motivation for our research.

### A. Description of the Concept

A schematic representation of the FARAD concept is shown in Fig. 1. It consists of two joined cylindrical Pyrex tubes. The smaller one (to the left in Fig. 1) serves for plasma generation while the adjoining larger-diameter vessel is where the acceleration takes place. Both vessels are surrounded by a set of applied  $B$ -field electromagnet coils. The magnet has been configured to produce a highly *axial* field inside the smaller tube and a highly diverging and mostly *radial* field near the flat back-end of the larger vessel, as shown by the representative applied  $B$ -field line drawn in the figure.

Gas (presently argon) is injected into the smaller tube (from the left in the picture) and is ionized by a helicon discharge, which requires an axial magnetic field and an RF antenna; the latter is wrapped around the *outside* of the tube as shown in the schematic. A helicon discharge[1–3] is a

radio-frequency inductive discharge that is very efficient as a plasma source. The highly ionized plasma is then guided by the magnetic field to flow radially outward along the inside of the flat back-end of the adjoining larger vessel.

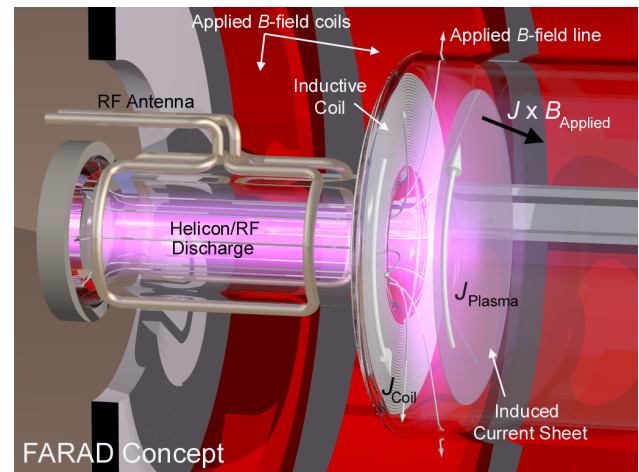


FIG. 1: Schematic illustration of the FARAD concept.

There is a flat inductive coil mounted on the outer side of the back-end (which protects the coil from the plasma) extending from the inner radius of the central opening to the outer radius of the larger vessel (called the acceleration stage). A large azimuthal current, labeled  $J_{\text{Coil}}$  in Fig. 1, is quickly pulsed through the coil. For a high-enough current rise rate ( $dI/dt \geq 10^{10}$  A/s) this pulse induces a current sheet in the plasma[4], which initially forms parallel and very close to the back-end.

The current sheet, shown as a thin disk in the figure, contains an induced azimuthal current, labeled  $J_{\text{Plasma}}$ , which flows in the opposite direction to the current in the coil.

\*Chief Scientist at EPPDyL. Associate Professor, Applied Physics Group. Associate Fellow AIAA.

†Graduate Research Assistant. National Defense Science and Engineering Graduate Fellow. Member AIAA.

‡Presented at the 40<sup>th</sup> AIAA/ASME/SAE/ASEE Joint Propulsion Conference and Exhibit, Ft. Lauderdale, FL. Copyright © 2004 by the authors. Published by the AIAA with permission.

The induced current density,  $j_\theta$ , interacts with the applied magnetic field resulting in a Lorentz body force, labeled  $\mathbf{J} \times \mathbf{B}_{\text{Applied}}$  in the figure. The resulting force density has two components: the first,  $j_\theta B_r$ , is axial and acts to accelerate the plasma downstream while the second,  $j_\theta B_z$  (due to the smaller but finite  $z$ -component of the applied magnetic field) is radial and acts to confine the plasma away from the wall, thus reducing wall losses. The thrust is due to the action of this Lorentz force density vector *and* the magnetic pressure that builds up between the back-end and the sheet and drives the latter downstream.

## B. Advantages and Motivation

The FARAD concept shares only one basic feature with a previous concept, namely the Pulsed Inductive Thruster (PIT)[5–7]. That feature is the inductive production of a current sheet via an external coil. The plasma production, mass injection, and plasma acceleration mechanisms are all substantially different from the PIT. FARAD also offers many advantages over existing concepts including the PIT.

It is helpful to contrast the PIT with the FARAD concept showing the advantages of the latter.

- In the PIT, a neutral gas is injected from a large nozzle located downstream of the thruster onto a very large coil (on the order of 1 m in diameter). That coil needs to be large in order to produce the required azimuthal electric field for gas breakdown ( $\sim 10$  kV/m) while maintaining an acceleration stroke of appreciable length relative to the gas depth thickness ( $\sim 7$ -10 cm). In FARAD, there is no such requirement on the electric field strength. The plasma is produced *independently* and efficiently in the RF stage of the device (the helicon source) which has a diameter of only a few centimeters (6 cm in the present experiment but can be made smaller). *FARAD is therefore inherently a much more compact device than PIT.*
- In FARAD, the applied magnetic field needed for the helicon source can be put to unique and advantageous uses.
  - First, it is used to *passively* bring the plasma produced in the helicon source *upstream of the acceleration stage* to the back-end of the acceleration stage, i.e. to the surface of the acceleration coil. This is in sharp contrast to the PIT where mass injection of the coil is through a physical and sizable nozzle (greater than 30 cm in diameter) that remains at all times in the accelerated plasma flow.
  - Second, by a judicious design of the applied magnetic field topology, the magnetic field lines can be made mostly radial in the immediate vicinity of the back-end (where most of

the acceleration takes place). The interaction of the radial component of  $B$  with the azimuthal current induced in the sheet provides an acceleration force density which is *in addition* to the magnetic pressure that builds up between the sheet and the coil and is the sole acceleration mechanism in the PIT<sup>1</sup>.

- A third advantage of the applied magnetic field is the role of the  $j_\theta B_z$  Lorentz force density component, mentioned above, in confining the plasma away from the walls, significantly decreasing wall losses and beam divergence.

The FARAD also offers the following general advantages over other existing electric propulsion concepts:

- FARAD is completely electrodeless. Both the RF antenna needed for the helicon source and the pulsed acceleration coil are not in contact with the working fluid. This mitigates the lifetime issues associated with electrode erosion (chemical reactions and sputtering, as well as spot-attachment induced melting and evaporation of electrodes) in electric thrusters.
- Related to the above advantage is the compatibility of the FARAD concept with a wide variety of propellants since their compatibility with metallic electrodes is not an issue. Water vapor, for instance, may prove to be a viable propellant (although its use in helicon discharges has not been explored). (Ne, Ar, He, Kr, H<sub>2</sub>, SiH<sub>4</sub>, O<sub>2</sub>, Cl, F and Xe have all been used successfully in helicon sources.)
- The separation of the ionization and acceleration stages, the ionization efficiency of the helicon source, and the reliance on the magnetic field to guide and supply the working plasma to the acceleration stage, result in a significant decrease of the fraction of neutrals in that stage. This should translate into high mass utilization efficiency.
- Since it is a purely electromagnetic accelerator, the FARAD does not suffer from the space charge limitation of electrostatic devices (which limits the thrust density) nor is it subject to the exhaust velocity limitations inherent to electrothermal devices (due to the requirement of tolerable thermal fluxes).
- While the detachment of plasma from magnetic field lines is a critical problem in some applied field propulsion concepts where the ions are magnetized and energized *along* the magnetic field lines, in the FARAD the ions are accelerated electromagnetically

<sup>1</sup> An equivalent interpretation of the magnetic pressure effect in the PIT is the repulsion between the current sheet and the coil which carry azimuthal currents of opposite directions. This, of course, does also happen in the FARAD but it is not the sole acceleration mechanism

by Lorentz body forces that are *always* perpendicular to the  $B$ -field. This is similar to the case of applied-field MPDTs[8, 9] where plasma detachment and thrust production have been demonstrated by many experiments.

- FARAD is an inherently pulsed device. Therefore it has the advantage of operating at a finite duty cycle from an arbitrarily low steady-state power and can thus, conceptually, be used on both high-power and low-power spacecraft. Furthermore, if the burst-pulse scheme of operation developed for gas-fed pulsed plasma thrusters[10, 11] is employed, FARAD can benefit from the high propellant utilization of that scheme and is largely free from the complication and lifetime limitations associated with fast acting valves<sup>2</sup>.

The outline for the rest of the paper is as follows. In section II the FARAD proof-of-concept experiment is described. Visual observations and probe data obtained using this apparatus are presented and discussed in section III.

## II. FARAD PROOF-OF-CONCEPT EXPERIMENT

The different components of the FARAD proof-of-concept experiment are described below. These components are assembled to form a dedicated experimental facility (shown in Fig. 2).

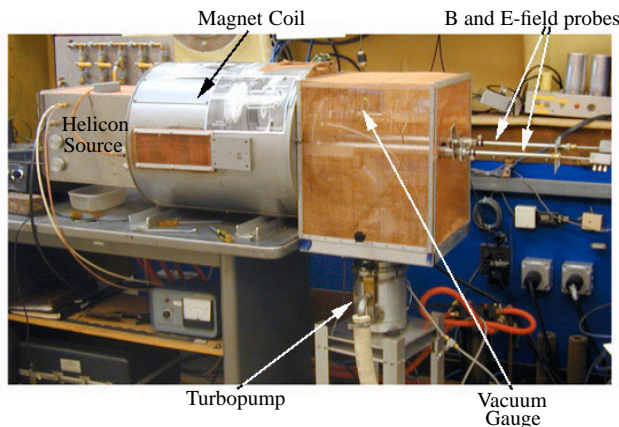


FIG. 2: Photograph of the facility used for the FARAD proof-of-concept experiment. The picture shows the water-cooled electro-magnet, Faraday cage, turbopump and associated equipment. The plasma helicon source is located inside the box on the left hand side.

<sup>2</sup> In this burst-pulse mode, a “slow” and sturdy valve is operated at a low duty cycle and the thruster is operated in a burst of discharge pulses, with a  $\Delta t$  between each consecutive *pulse* equal to the time it takes the current sheet to sweep the gas through the thruster. The time between the *bursts* is dictated by the available steady-state power and the required (average) thrust.

### A. Vacuum Vessel

The vacuum vessel consists of two Pyrex cylinders placed inside of a 0.1 Tesla magnet. The small cylinder is 6 cm in diameter and 37 cm in length while the large cylinder is 20 cm in diameter and 46 cm in length. The cylinders are connected using a G-11 (fiberglass) plate with a 6 cm concentric hole at the center to allow free flow of gas between the two cylinders. An induction coil (used to accelerate the plasma) is mounted to the G-11 plate inside the vacuum chamber. A photograph of the small cylinder mated to the G-11 plate is shown in Fig. 3.

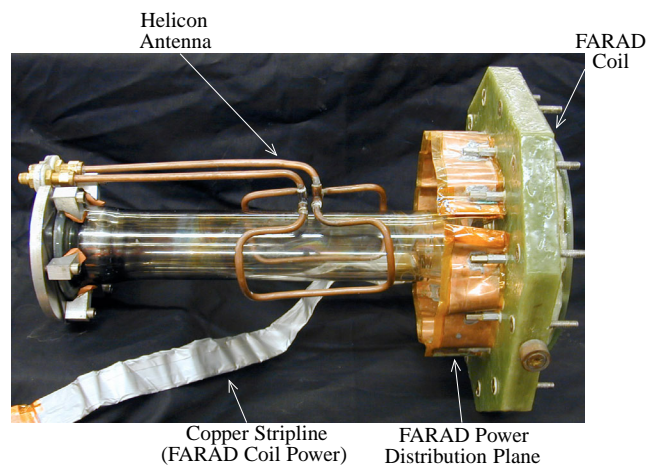


FIG. 3: Side view of the fully assembled FARAD proof-of-concept experiment. This photograph can be compared directly to the conceptual schematic shown in Fig. 1.

A constant background pressure (0.1 to 55 mTorr) is maintained by a gas feed located at the endplate of the large cylinder and by a 150 l/s turbo pump with a conductance controller backed by a roughing pump. A background pressure of  $5 \times 10^{-6}$  Torr can be maintained while the turbo pump is operating and the conductance controller is in the open position. All experiments presented in this paper were performed with argon.

### B. Applied Magnetic Field

The applied magnetic field is generated using a Varian VA-1955A klystron magnet. No effort at this proof-of-concept stage has been made to develop a compact magnet that would be more ideal for an actual thruster. This apparatus contains five separate, water-cooled magnetic coils (see schematic in Fig. 4). The magnet wiring has been altered to allow the currents in coils 1, 2 and 3 and coils 4 and 5 to be driven in opposite directions by two different power supplies. By flowing current in opposite directions in the different coil sets, a cusp in the magnetic field can be created. Two Electronic Measurements EMCC 120-40 power supplies provide current to the coils.

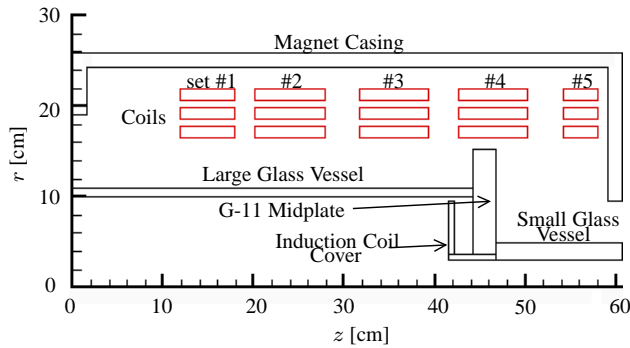


FIG. 4: An axisymmetric schematic depicting the geometry of the magnet and vacuum vessel (to scale).

1. Magnetostatic Modeling

A 2-D axisymmetric numerical model of the magnet and case was constructed and solved using the Maxwell SV magnetostatic modeling program (Ansoft Corp., Pittsburgh, PA). The model is shown to scale in Fig. 4. The coil sets consist of three separate, concentric, toroidal copper rings. Each ring carries an equal amount of the total assigned current. The magnet case is modeled with a relative magnetic permeability of 60. As in the experiment, the currents in coil sets 1, 2 and 3 flow in the same direction. Coil sets 4 and 5 are driven by a separate power supply in the opposite direction.

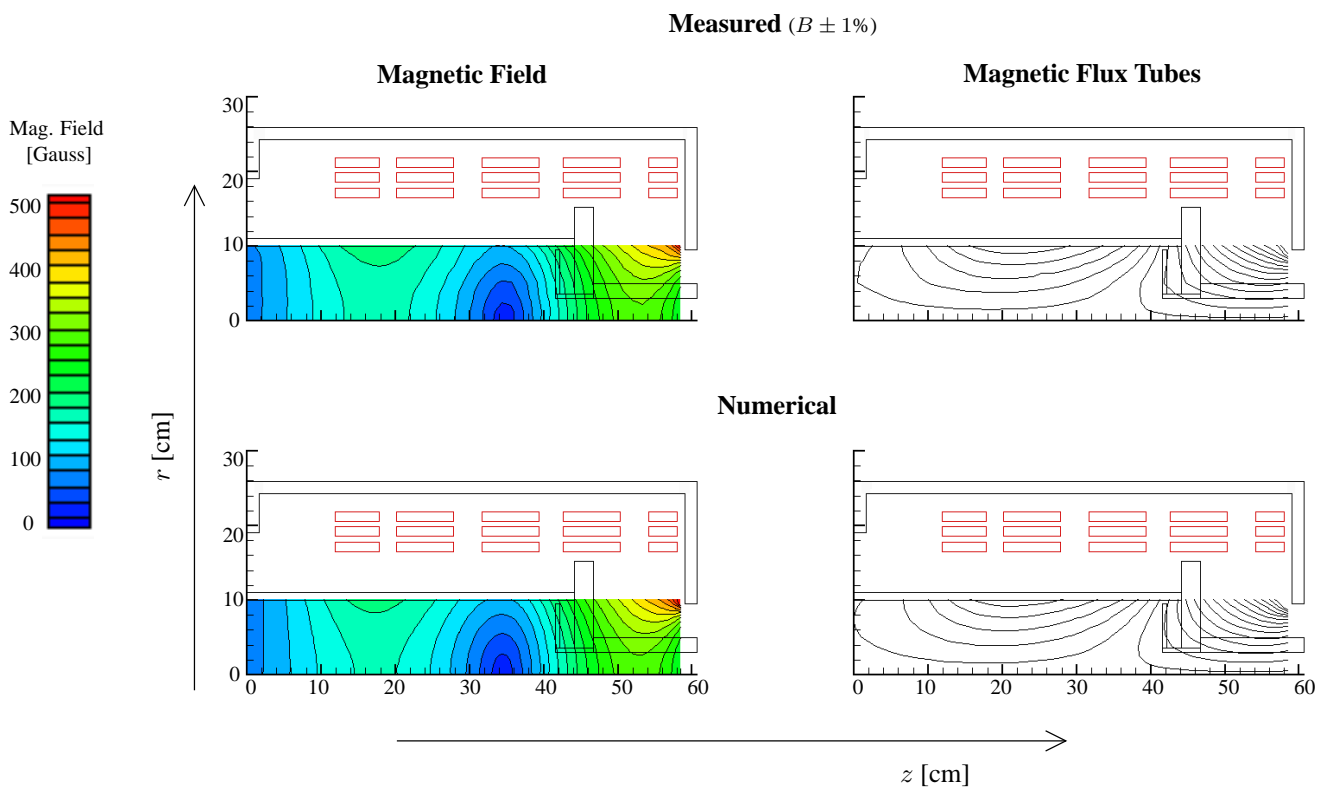


FIG. 5: Applied magnetic field measurements (top) and modeling results (bottom) for the case where the current in coils 1-3 = 10.2 Amps and the current in coils 4-5 = 23.9 Amps, showing excellent agreement.

2. Applied Field Measurements

Measurements of the steady-state magnetic field in the coil were performed using an FW Bell gaussmeter (model 5080) calibrated to an accuracy of 1%. The axial and radial components of the field were measured on a grid with spacings in both the axial and radial directions of 1.27 mm (1/2"). This grid covers 10.16 mm (4") in the radial direc-

tion and 58.42 mm (23") in the axial direction. The current provided by the power supply for coils 1-3 was 10.2 Amps while the current for coils 4 and 5 was 23.9 Amps. The results of this measurement are given in the top half of Fig. 5 while the bottom half of the same figure shows results predicted by the magnetostatic model operating under the same conditions. The agreement with the model is excellent as the calculated and measured maps are almost indistinguishable.

### C. Plasma Generation

A Boswell-type saddle antenna (helicon antenna)[12] is placed around the small cylinder (shown on the left side of Fig. 3) and used to generate the plasma. The antenna is constructed of copper tubing to allow water cooling during operation. The helicon discharge[1–3] is produced by supplying power (steady-state or pulsed) to the antenna from an ENI 13.56 MHz, 1.2 kW power supply through a tuner. The tuner consists of an L network composed of two Jennings 1000 pF, 3 kV variable vacuum capacitors. It is located as close to the antenna as possible to maximize coupling.

Inductive discharges are easily obtained using only a few watts of forward RF power to the antenna, however to ignite a helicon discharge the power level must be raised to at least 500 Watts. The inductively coupled discharge is homogeneous and occupies the entire cross section of the small cylinder. The helicon discharge also occupies the entire tube, but it is most intense along the cylinder centerline where a bright blue column is observed.

Special precaution has been taken in choosing the back-plate material for the antenna side. In our case, molybdenum is used to minimize sputtering.

The RF source produces a steady-state plasma which follows the magnetic field lines. As it reaches the back-end of the acceleration region the plasma forms a circular slab, spreading radially over the face of the induction coil. At this point, it is ready for subsequent acceleration by the FARAD induction coil.

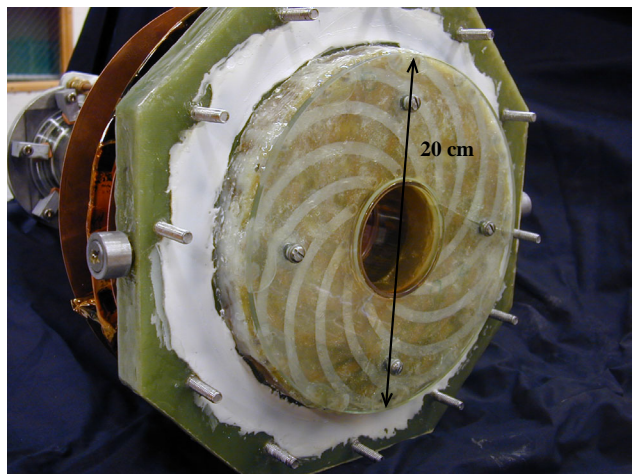


FIG. 6: Skewed end view of the fully assembled FARAD experiment showing the face of the acceleration coil.

### D. Acceleration Coil

The FARAD acceleration coil (seen in Fig. 6) is similar to the Marx-type coil used by Lovberg and Dailey in later generations of the PIT[6]. However, it is quite different in scale and pulse energy. The PIT MkV coil is comprised

of 18 half-turn coils, has an outer diameter of 1 meter and operates at roughly 4 kJ/pulse. The FARAD, on the other hand, possesses 12 half-turn coils, has an inner diameter of 20 cm and has been operated at up to 78.5 J/pulse.

The half-turn coils are connected in parallel using copper strips. A 39.2  $\mu\text{F}$  capacitor is remotely located and connected to the coil using copper stripline. Current is switched using a simple contact, or “hammer”, switch. In a real thruster, SCRs or some other type of solid-state switching could be used. A circuit schematic of the acceleration stage, showing both the driver circuit and the inductively coupled plasma, is shown in Fig. 7.

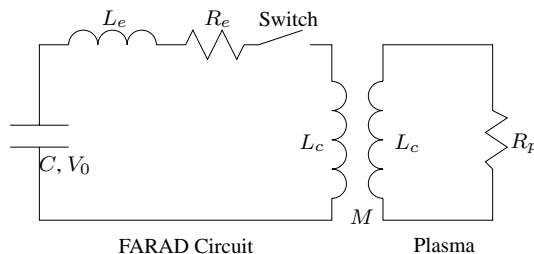


FIG. 7: Circuit schematic of the FARAD acceleration coil and the coupled plasma.

## III. PROOF-OF-CONCEPT EXPERIMENT

During operation of the FARAD proof-of-concept experiment, a helicon plasma is initiated and allowed to reach a steady-state condition. The duration of the helicon discharge prior to pulsing the acceleration coil is  $\sim 1$ -2 secs. The helicon source remains active well after the acceleration pulse ( $\mathcal{O}(1-10) \mu\text{s}$ ) is complete.

We note here that in a real thruster care should be taken in choosing both the correct pulse widths and the inter-pulsing scheme. There are three major pulsed systems in the FARAD concept (the applied  $B$ -field being left in a steady-state mode):

1. The neutral gas pulse, of temporal extent  $\Delta t_g$ , precedes the other pulses and should be long enough to fill the helicon stage with neutral gas but short enough to avoid leaking gas that will not be accelerated.
2. The RF pulse,  $\Delta t_{\text{RF}}$ , is the duration of the power supplied to the helicon stage. While the helicon stage can be operated in a steady-state mode (as we have done in the proof-of-concept experiment), it must be operated in a pulsed mode in a real thruster since the acceleration mechanism itself is pulsed. In a real thruster the RF pulse is not started until the injected gas has filled the helicon stage and must end late enough to allow most of the produced plasma to migrate to the back-end of the acceleration stage but early enough to avoid producing extraneous plasma that may not participate in the acceleration process.

- The acceleration coil pulse,  $\Delta t_{ac}$ , must not start until most of the plasma has been guided to the back-end of the acceleration stage and must not end until the current sheet has traveled an axial distance  $l_{emc}$  which represents the axial extent, from the back-end, of the region in which electromagnetic coupling between the sheet and the coil occurs. For axial locations  $z \geq l_{emc}$  the current sheet is decoupled from the acceleration coil and survives only on a time scale on the order of the recombination time scale,  $t_{rec}$ .

While we have not performed any optimization of these parameters in the proof-of-concept experiment, it is clear that the pulse inter-sequencing and relative magnitude of  $\Delta t_g$ ,  $\Delta t_{RF}$ ,  $\Delta t_{ac}$  and  $t_{rec}$  will have significant impact on both the mass utilization efficiency and the propulsive performance of a real thruster.

### A. Visual Observations

A simple visual observation provided verification of the passive magnetic-field-guided plasma injection onto the acceleration coil. The helicon plasma is quite luminescent and can be seen following the applied magnetic field lines and spreading over the acceleration coil (see Fig. 8).

Also, a visual observation provided evidence of current sheet formation. When current is pulsed through the acceleration coil, a very bright ‘flash’ of light appears in a thin region near the coil. The flash is homogeneous over the face of the coil and its intensity temporarily overwhelms the light emitted by the steady-state (helicon) plasma. The short duration, bright light emission is most likely indicative of increased ionization and current sheet formation across the coil face.

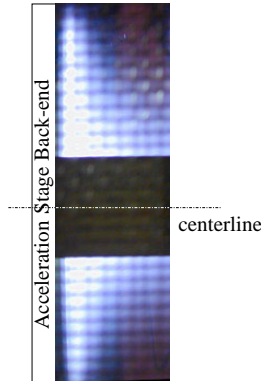


FIG. 8: Photograph of the steady-state RF plasma as it follows magnetic field lines and spreads out over the face of the FARAD coil (through a 1.0 neutral density filter). The bright area adjacent to the back-end, where the acceleration coil is located, is emission from the injected plasma. The grid pattern in the picture is due to the mesh of the Faraday cage enclosing the experiment.

### B. Current Monitoring

The current flowing through the acceleration coil,  $J_{Coil}$ , is monitored using an air-core Rogowski coil[13]. The raw probe output, which is proportional to the derivative of the enclosed current, is integrated numerically to yield a current waveform. The error on the calibration constant, which multiplies the integrated Rogowski coil waveform, is  $\pm 3\%$  and the integration errors have been estimated to add an additional 2% error for a total of  $\pm 5\%$ .

A typical current waveform of driver circuit is given in Fig. 9. Since the fractional change in the inductance is low ( $\Delta L/L_0 \approx 10\%$ ), the current in the coil is roughly the same with or without a current sheet present. The maximum  $dI/dt$  in our circuit is roughly  $1.8 \times 10^{10}$  A/s, which is the level required to form a plasma current sheet[4].

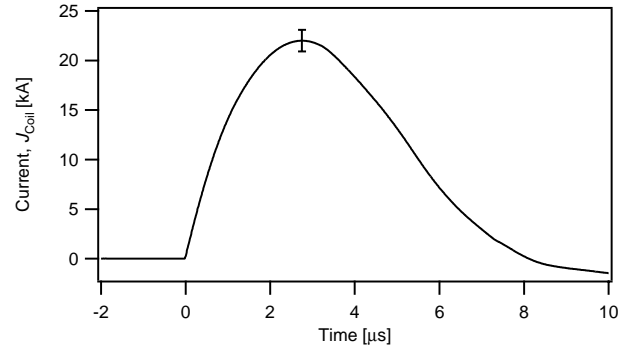


FIG. 9: Total current in the acceleration coil,  $J_{Coil}$ , (with a typical error bar) for a pulse energy of 78.5 J.

### C. Magnetic Field

#### 1. Applied Field

The values of the applied (steady-state) magnetic field have been computed numerically using a realistic magnetostatic model. For completeness, plots of the variation of the applied field ( $B_r$  and  $B_z$ ) along an axial line at a radius of 66 mm are given in Fig. 10. In the model, coils 1-3 were supplied with 36.5 Amps while 38 Amps were delivered to coils 4-5 by the power supply. These numbers match those used during the experiments. The  $B_r$  field peaks just in front of the coil while the  $B_z$  field goes to zero, as expected.

#### 2. Induced Field

The induced (time-varying) magnetic field measurements are acquired using  $B$ -dot probes[14]. Three Panasonic 220 nH wire-wound non-magnetic core surface mount inductors are used to measure  $dB/dt$  in three orthogonal directions (note that the orientation of the probe

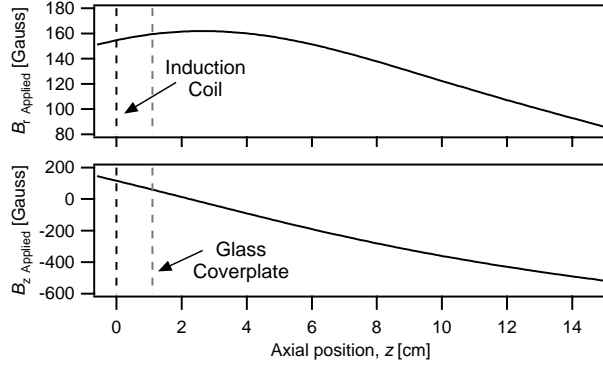


FIG. 10: Calculated applied magnetic field strengths in the  $r$  and  $z$  directions in front of the acceleration coil at a radius of 66 mm. The coil position ( $z = 0$ ) and the edge of the glass plate covering the coil are sketched in the plot.

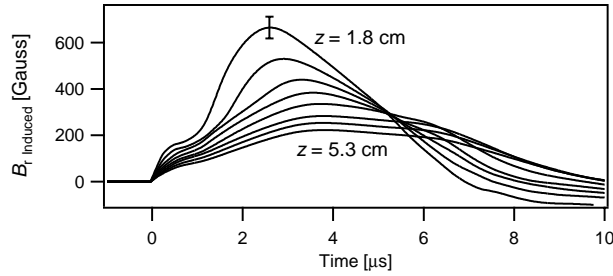


FIG. 11: Time histories of the measured induced radial magnetic field strengths (with a typical error bar) along an axial line at a radius of 66 mm. The axial positions are spaced evenly every 5 mm. The discharge energy was 78.5 J and the background pressure was 23 mTorr.

is not the same as the  $r$ - $\theta$ - $z$  coordinate system in which our data is presented). The  $dB/dt$  signals were numerically integrated in time, multiplied by their respective calibration constants, and linearly combined to obtain  $B(t)$  in the  $r$ - $\theta$ - $z$  coordinate system. The maximum error on the calibration constants is  $\pm 5.4\%$  and the maximum error on the measurement of  $B_r$  is  $\pm 7\%$ .

A plot showing the temporal and spatial variation of the induced magnetic field at a radius of 66 mm is presented in Fig. 11. The axial,  $z$ , locations are evenly spaced every 5 mm between 1.8 cm and 5.3 cm from the coil face. A few points should be made regarding this plot. First, the traces all begin increasing immediately at  $t = 0$ . This feature has been previously observed in pulsed inductive devices [5, 15] and indicates that initially the field induced by the coil rapidly diffuses through the plasma, implying low initial conductivity. Another observable feature in the waveforms is a distinct ‘knee’ in the radial magnetic field. This feature is directly attributable to the current sheet and its origin and meaning are discussed below.

### 3. Discussion

The induced magnetic field in any pulsed inductive discharge has two sources (see Fig. 12). The first is the current,  $J_{\text{Coil}}$ , being driven through the induction coil, while the second is the current sheet induced in the plasma,  $J_{\text{plasma}}$ . The measure of the induced magnetic field acquired using  $B$ -dot probes is a linear superposition of these two fields.

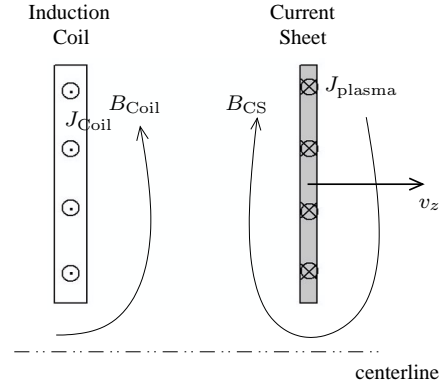


FIG. 12: Schematic representation of the driver circuit and induced current sheet and their associated contributions to the magnetic field.

The magnetic field components,  $B_r$  and  $B_z$ , induced by the current flowing in the coil,  $J_{\text{Coil}}$ , are directly proportional to that current, in accordance with the Biot-Savart law,

$$d\mathbf{B} = \frac{\mu_0 I d\mathbf{L} \times \hat{\mathbf{r}}}{4\pi r^2}, \quad (1)$$

where  $I$  is the current flowing through an element of length  $d\mathbf{L}$  and  $\hat{\mathbf{r}}$  is the unit vector specifying the direction of the vector  $\mathbf{r}$ , which points from the current element to the field point. It is important to note that the solution for any scalar component of the induced field always has the form  $B \propto I$ , where all of the geometric information in the problem is contained within the proportionality constant. Once this constant is known for any given point, either through a calibration or a detailed computation based upon Eq. (1), the induced field due to  $J_{\text{Coil}}(t)$  can be calculated. While unintentional, one of the benefits of having a low fractional change in circuit inductance over the acceleration stroke length was that  $J_{\text{Coil}}(t)$  (and the induced magnetic field) are essentially unchanged by the presence of a current sheet. As such, a magnetic field trace obtained when no plasma was present is taken as the contribution of  $J_{\text{Coil}}$  to the total induced magnetic field.

Waveforms showing the contributions to the magnetic field due to the induction coil and the current sheet are shown in Fig. 13. The current sheet contribution has been inferred by subtracting the contribution due to the coil from the total measured field.

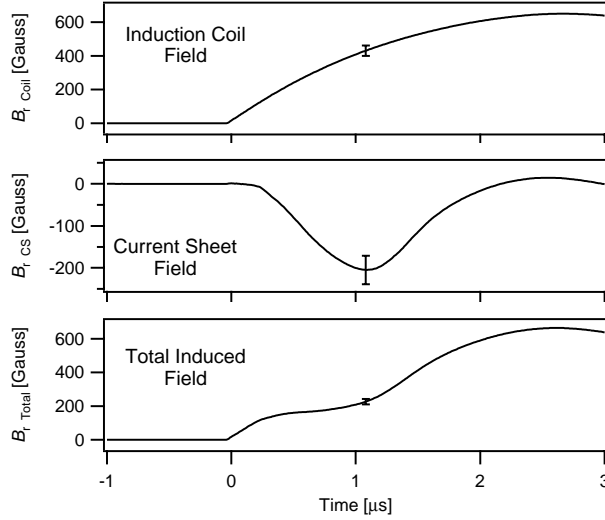


FIG. 13: Measured radial magnetic field contributions of the induction coil and the current sheet to the total induced field ( $z = 1.8$  cm). The discharge energy was 78.5 J and the background pressure was 23 mTorr. (Typical error bars shown for the time where  $B_{r,CS}$  is minimum.)

While the data provides a qualitative indication of the presence and effect of a current sheet, magnetic field maps along a single axial line *are not* a good method for determining a current sheet's exact position, velocity and strength in an inductive accelerator. While a clear minimum does exist in the plots of the current sheet contribution to the induced field (see Fig. 13, center plot) there is a great deal of ambiguity in interpreting this minimum.

The situation for an inductive accelerator is considerably more complicated than that found in non-inductive (direct discharge) pulsed plasma accelerators where the plasma completes the only circuit in the device[16]. In the inductive case, the sheet is created by the interaction of  $d\mathbf{B}_{CS}/dt$  with the plasma through Faraday's law,

$$\nabla \times \mathbf{E} = -\frac{d\mathbf{B}_{CS}}{dt},$$

where the induced electric field,  $\mathbf{E}$ , drives the current flowing in the sheet. This implies that the sheet strength is dependent upon  $dJ_{Coil}/dt$  through Eq. (1). However, the sheet also decouples from the induction coil as its axial distance,  $z$ , from the coil increases. As either  $dJ_{Coil}/dt$  decreases or  $z$  increases, the induced current sheet weakens. The rate at which the sheet strength is changing cannot be deconvolved from the rate at which it is approaching a given point for a series of measurements along a single line. A minimum in the plot of  $B_{CS}$  could be due to either effect.

One solution to this problem is to measure the magnetic field in a two-dimensional  $r$ - $z$  plane and use Ampère's law,

$$\nabla \times \mathbf{B} = \mu_0 \mathbf{j},$$

to compute the current density,  $\mathbf{j}$ , in the sheet. The only portion of the magnetic field in the region of interest that

is not curl-free is that part attributable to the current sheet. This measurement will, therefore, unambiguously yield the sheet position and strength as a function of position and time and will be carried out in future experiments.

#### D. Current Sheet Visualization

Visualization of the current sheet formation and subsequent motion is accomplished using a Hadland Photonics Imacon 792/LC fast-framing camera. The photographs are obtained using a 20 million frames per second module, with each frame having an exposure time of 10 ns. No filtering was used to obtain these photographs, so any light emission that was bright enough is seen. However, the RF/helicon plasma did not produce enough light on its own to appear in any of our photographs, thus the light in each exposure corresponds to emission from the current sheet. Due to obstructions in the optical path only one region of the plasma, extending some 20 mm radially, is shown in the photographs in Fig. 14.

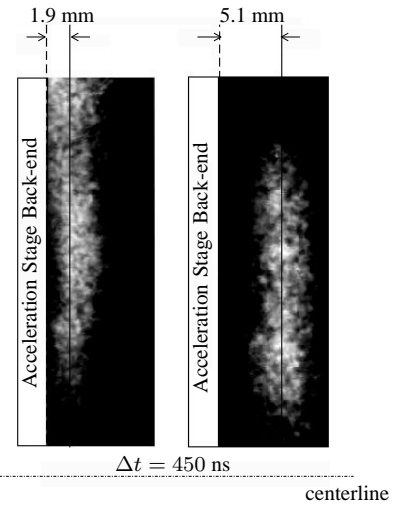


FIG. 14: High-speed photographs acquired using a fast-framing camera at a framing rate of 20 million frames per second showing the current sheet formation (left panel) near the back-end of the acceleration stage and the sheet's position 450 ns later (right panel). (The contrast in these photographs has been enhanced through digital image processing.) The inferred velocity is approximately 7.1 km/s.

The photographs presented show the current sheet (for a driver circuit having  $C = 3 \mu\text{F}$ ,  $V_0 = 2$  kV and  $\Delta L/L_0 \approx 30\%$ ) during an early stage of its evolution after it has formed along the back-end of the acceleration region (left panel) and at a time 450 ns later when it has moved about 3.2 mm further downstream. A rough estimate of the sheet velocity based on these pictures is approximately 7.1 km/s. It is important to note that *this does not represent the typical exhaust velocity of the FARAD concept* because 1) no effort was made to optimize the acceleration process, 2) the sheet may have reached its peak velocity and de-

celerated due to neutral drag and 3) no photographs have yet been acquired at discharge energies greater than 6 J. In this proof-of-concept experiment, we refrain from making quantitative projections of the propulsive performance of FARAD.

Finally, it is interesting to note, from the same photographs, that the sheet has moved radially towards the center axis (located below the bottom edge of the photographs) as would be qualitatively expected under the effect of the radial component of the Lorentz force ( $j_{\theta} B_z$ ) whose presence and confining action (reducing wall losses) are main features of the FARAD concept.

#### IV. CONCLUSIONS

We have presented a new RF-assisted pulsed inductive accelerator concept, FARAD, and described a proof-of-concept experiment. The following conclusions can be made regarding the conceptual design of such a device and the experimental results:

- By decoupling the ionization and acceleration processes, the FARAD can be scaled to lower operating voltages and smaller physical sizes than previous pulsed inductive accelerator concepts.
- The FARAD advantages include efficient plasma production, mass injection directed along applied magnetic fields, and electromagnetic acceleration realized through an interaction between the induced

current sheet and *both* the induced and applied magnetic fields.

- A proof-of-concept experiment possessing a low fractional change in circuit inductance (i.e. not optimized as a thruster) has been used to show coupling between the preionized plasma and the acceleration coil.
- Visual observations in the proof-of-concept experiment indicate that the pre-ionized plasma follows magnetic field lines and forms a plasma slab on the face of the acceleration coil. Also, when current is pulsed through the acceleration coil, a bright flash on the coil surface is visible to the naked eye. This bright flash is, most likely, indicative of increased ionization and current sheet formation.
- Magnetic field probing along a single axial line gives qualitative evidence of the presence and effect of a current sheet.
- Visualization using a fast-framing camera provides an observation of the formation of the current sheet and its acceleration to a velocity of 7.1 km/s.

#### Acknowledgments

We gratefully acknowledge R. Spektor for the aid he provided during the performance of these experiments. We also acknowledge R. Sorenson, J. McQuade, T. Crowley and B. Beck for their contributions to this work.

- 
- [1] F.F. Chen and R.W. Boswell. "Helicons - The past decade". *IEEE Trans. Plasma Sci.*, **25**(6):1245, Dec. 1997.
  - [2] R.W. Boswell and F.F. Chen. "Helicons - The early years". *IEEE Trans. Plasma Sci.*, **25**(6):1229, Dec. 1997.
  - [3] J.A. Lehane and P.C. Thonemann. "An experimental study of helicon wave propagation in gaseous plasma". *Proc. Phys. Soc.*, **85**:301, 1965.
  - [4] R.G. Jahn. *Physics of Electric Propulsion*. McGraw-Hill Book Company, 1968. pp. 286.
  - [5] C.L. Dailey and R.H. Lovberg. *PIT clamped discharge evolution*. Technical Report AFOSR-TR-89-0130, TRW Space and Technology Group, Dec. 1988.
  - [6] C.L. Dailey and R.H. Lovberg. *The PIT Mkv pulsed inductive thruster*. Technical Report NASA CR-191155, TRW Systems Group, July 1993.
  - [7] C.L. Dailey and R.H. Lovberg. "Current sheet structure in an inductive-impulsive plasma accelerator". *AIAA Journal*, **10**(2):125-129, Feb. 1972.
  - [8] D.B. Fradkin. *Analysis of acceleration mechanisms and performance of an applied field MPD thruster*. PhD thesis, Dept. of Mechanical and Aerospace Engineering, Thesis No. 2052-T, Princeton University, Princeton, NJ, 1973.
  - [9] G. Krulle, M. Auweter-Kurtz, and A. Sasoh. "Technology and application aspects of applied field magnetoplasmadynamic propulsion". *J. Propuls. Power*, **14**(5):754-763, 1998.
  - [10] J.K. Ziemer, E.A. Cubbin, E.Y. Choueiri, and D. Bix. "Performance characterization of a high efficiency gas-fed pulsed plasma thruster". In *33<sup>rd</sup> Joint Propulsion Conference*, Seattle, Washington, July 6-9, 1997. AIAA 97-2925.
  - [11] J.K. Ziemer, E.Y. Choueiri, and D. Bix. "Trends in performance improvements of a gas-fed pulsed plasma thruster". In *25<sup>th</sup> International Electric Propulsion Conference*, Cleveland, OH, 1997. IEPC 97-040.
  - [12] A.R. Ellingboe, R.W. Boswell, J.P. Booth, and N. Sadeghi. "Electron beam pulses produced by helicon-wave excitations". *Phys. Plasmas*, **2**(6):1807, June 1995.
  - [13] Wright, E.S. "The design and development of Rogowski coil probes for measurement of current density distribution in a plasma pinch". Report No. 740, Dept. of Aerospace and Mechanical Sciences, Princeton University, Princeton, NJ, June 1965. Also M.S.E. Thesis, May, 1965.
  - [14] R.H. Lovberg. "Magnetic probes". In R.H. Huddleston and S.L. Leonard, editors, *Plasma Diagnostic Techniques*, pages 69-112. Academic Press, New York, 1965.
  - [15] R.H. Lovberg and C.L. Dailey. "Current sheet development in a pulsed inductive thruster". In *25<sup>th</sup> Joint Propulsion Conference*, Monterey, CA, July 10-12, 1989. AIAA 89-2266.
  - [16] J.W. Berkery and E.Y. Choueiri. "Characterization of current sheet evolution in a pulsed electromagnetic accelerator". In *28<sup>th</sup> International Electric Propulsion Conference*, Toulouse, France, 2003. IEPC 03-307.